Journal of Heat and Mass Transfer Research 7 (2020) 165- 176

Journal of Heat and Mass Transfer Research

Journal homepage: http://jhmtr.semnan.ac.ir

Semnan University

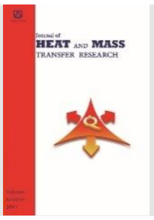

Longitudinal Vortex Rolls in Fluids

Takeo R.M. Nakagawa[*], **Ai Nakagawa**

Academy of Hakusan, 2-14, Meiko, Hakusan 920-2152 Japan.

PAPER INFO

Paper history:
Received: 2020-08-10
Accepted: 2020-10-16

Keywords:
Thermal Convection;
Longitudinal Roll;
Heat Transfer;
Vortex in Nature;
Flow in Box.

ABSTRACT

The Rayleigh-Bénard problem of a horizontal fluid layer with different boundary conditions has been explored to acquire the basic knowledge on longitudinal vortex rolls in nature. Conducted are two experiments on flow visualization with neutral buoyant particles, and measurements of flow velocity and heat transfer rate caused by the thermal convection between two coaxial square containers, which are set horizontal and inclined by 45°, respectively. It is found that the critical Rayleigh number Ra_c for the onset of the thermal convection in the horizontal top-section is equal to 1660±97, whereas, in the inclined by 45° top left test-section, it is smaller than 1300. The moving free boundaries towards upwards at each sides, respectively don't enhance the thermal convection, but contribute to induce the longitudinal alternating vortices arranged in the horizontal top test-section. On the one hand, by inclining the coaxial square containers by 45°, the heat transfer rate is significantly increased. It is suggested that longitudinal rolls in nature are generated by the essentially same origin and mechanism as those in the laboratory, though the former boundary conditions are often difficult to specify.

DOI: 10.22075/jhmtr.2020.21013.1299

1. Introduction

The buoyancy induced vortex flow structures at a high Gr/Re2 in a mixed convective flow by a bottom heated horizontal flat duct plays an important role in a number of technological processes such as cooling of microelectronic equipment, enhancing thermal efficiency of compact heat exchangers, collecting solar energy, generating longitudinal rolls, and many others(Femando 1991, Laein et al. 2016), where Gr is the Grashof number, and Re is the Reynolds number.

The vortex flow in a horizontal duct normally appears in the form of either longitudinal or transverse rolls depending on the Reynolds number Re. At a higher Gr/Re2, these vortex rolls become unsteady in time and space. Additionally, during the time and space development, the existing vortex rolls may merge or split so that new rolls may be generated. The detailed understanding of these complicated temporal-spatial structure change is critical to improve the thermal design of various engineering systems, and is especially important in growing a pure crystal from the vapor phase. The changes in vortex structures are rather drastic in a duct when the aspect ratio (width/length) is large, for it provides more space for the rolls to move towards the span-wise direction.

The onset of the secondary flow owing to thermal instability in mixed convection in a horizontal plane channel has been found to be at the Rayleigh number Ra=ca.1708 by Akiyama et al. (1971) and Kamotani et al. (1979). This result is consistent with the linear stability analyses (e.g. Lee et al. 1991). In the range beyond the critical value, steady longitudinal vortex rolls prevail, and so the span-wise temperature distribution shows the regular sinusoidal wavy shape, in which the roll number coincides with the aspect ratio (Akiyama 1971). However, the regular sinusoidal temperature distribution is distorted by increasing the Rayleigh number Ra > 8000 at the Reynolds number Re=38(Ostrach & Komatani 1975, Komatani & Ostrah 1976). The flow regime map of Re vs. Ra has been drawn by using the experimental results with nitrogen gas (Chiu & Rosenberger 1987) to specify the boundaries among (a) flow with no roll, (b) steady rolls, and (c) unsteady rolls. The vortex flow structure in the

---

[*] *Corresponding Author: Takeo R.M. Nakagawa, Academy of Hakusan, 2-14, Meiko, Hakusan 920-2152 Japan.*
Email: takeonakagawa8@gmail.com

thermal boundary layer is found to be influenced not only by the Rayleigh number Ra but also the Froude number Re2/Gr (Komatani & Ostrach 1976). Furthermore, it should be noted that at very low Reynolds number Re, the flow in the duct is in the form of transverse vortex rolls (Quazzani et al. 1989, Quazzani 1990).

The main purpose of the present study is to seek for the universal principle on the onset of longitudinal rolls in nature, appearing commonly in sea, desert, and atmosphere theoretically and experimentally.

2. Longitudinal Rolls in Nature

In this section, longitudinal rolls in nature will be introduced by dividing the sea, desert, and atmosphere, respectively.

2.1. Sea

There are many direct observations of longitudinal vortices in the sea, where it is known as *Langmuir circulation* (Figures 1 and 2). Langmuir(1938) observed streaks of seaweed spaced 100~200m apart on the surface of the Atlantic Ocean, and they are oriented in the direction of the surface wind: It was suggested by Langmuir that this was the result of alternating left and right helical longitudinal vortices at the topmost ocean surface layer, as depicted in Figure 2. Additional observations of the motion of sheets of paper, and *sargassum weed* bands appeared on the sea surface have also made the confirmation on his viewpoint for this observation.

It is believed that these rows are generated by the vortex motion within the Langmuir cells at the surface layer of the sea, as depicted in Figure 2.

2.2. Desert

Let us consider longitudinal sand dunes, which cover over half the area of the large deserts of the world. As shown in Figure 3, the longitudinal but slightly meandering dunes are aligned in the prevailing wind direction and are spaced about 2km apart (Helga 2008). It is inferred that the sand bed is engraved along the sinuous loci which must be no more than those along the loci of the local maximum shear stress at each of the cross sections due to the flow of wind over the bed A possible mechanism for these dunes is that they are formed by large eddies in the atmosphere-counter-rotating roll vortices aligned along the wind direction with diameters approximately equal to the thickness of the atmospheric boundary layer, and the wavelengths are about three times this thickness, as depicted in Figure 4. This type of dune was first described by several anonymous observers in the Libyan deserts during the first three decades of the 20th century. It is said that one such an observer, King, W.J.H. describes it in an essay in scientific details as follows: “The most striking features of the Libyan desert are the curious long, narrow dune belts running across the desert, roughly from north to south, in almost straight lines.” The spacing of the dunes varies between 300m and 8km, and similar dune patterns have also been observed from airplanes over the Australian, Saudi Arabian, and Algerian deserts. Satellite photograph (Figure 3) has revealed the existence of longitudinal dune systems in nearly every large desert of the world. A remarkable feature of these systems is their continuity and geometric regularity. Commonly, smaller-scale dune structures appear on the surface of the larger dunes, as seen at the inset of Figure 3. Typically, a longitudinal dune is 20~50m high, at least 100m wide, and ranges in length from a few hundred meters to several hundred km.

2.3. Atmosphere

There are many direct observations of longitudinal vortices in the atmosphere. The long parallel cumulus cloud streets that appear often if weather is fine, have been believed to be manifestations of these longitudinal rolls below: The street is formed by the upward moving air between two convective flows, as depicted in Figure 6.

In cloud streets, it has been found that the average spacing of such features is between 5 and 10km, which is typically two or three times of the atmospheric convective layer. In general, the following conditions are desirable for the formation of cloud streets: (a) flat underlying terrain, (b) little variation of wind direction with height, (c) wind speed higher than normal, (d) strong curvature of the wind speed profile. Normally, the wind speed increases away from the surface, reaching a maximum at an altitude of about 1 km, and then decreases above this height. Finally, (e) the lapse rate of the temperature is unstable near the surface in such a way that the temperature decreases with altitude, rendering thermal convection possible.

It appears that these five conditions are frequently satisfied in the trade wind regions over tropical oceans, so that cloud streets are a common form of convective activity when the latitude is below 30°. Within these latitudes, most large deserts are to be found, and thus longitudinal vortices are to be expected over the deserts as well as the oceans. Indeed, satellite photographs indicate that cloud streets occur at all latitudes. Their spacing average of 1~10km, is consistent with those of longitudinal dunes.

3. Longitudinal Rolls in Laboratory

Let us start the Rayleigh-Bénard problem of a horizontal fluid layer heated from below, which is a mixed convective flow. This is characterized by the thermally unstable stratification in the gravitational field: The heavy cold fluid is above the light warm layer. The basic state in the flow is defined by the heat conduction. However, once the temperature difference between the horizontal two boundaries exceeds a certain critical value, buoyancy driven thermal convection starts, together with an additional transverse heat transport in the horizontal layer.

3.1. Basic Equations and Boussinesq Approximation

The convective transport processes and their instabilities are described by the basic equations of fluid mechanics. Bird et al. (1960) have shown that the conservation of mass, momentum, and energy in a homogeneous fluid produce the following system of partial differential equations,

$$\partial\rho/\partial t + \nabla\cdot(\rho v) = 0 \tag{1}$$

$$\partial(\rho v)/\partial t + [\nabla\cdot\rho vv] = -\nabla p - [\nabla\cdot\tau] - \rho g e \tag{2}$$

$$\partial\rho(U+\mathbf{v}^2/2)/\partial t + \nabla\cdot\rho\mathbf{v}(U+\mathbf{v}^2/2) = -\nabla\cdot\mathbf{q} + \rho g(\mathbf{v}\cdot\mathbf{e}) - \nabla\cdot(p\mathbf{v}) - \nabla\cdot[\tau\cdot\mathbf{v}] \tag{3}$$

The conservation of mass per unit volume (1) indicates that the temporal change of mass in a volume element is the same as the balance between inflow and outflow. In the same way, the momentum balance (2) shows that the rate of momentum accumulation is equal to the rate of momentum into and out of the volume element plus the pressure, viscous and gravitational forces acting on the system. The rate of gain of internal and kinetic energy (3) is in equilibrium with the convective rate of energy and the rate of energy by conduction, gravity, pressure, and viscous forces.

In the case of the Bénard convection of a horizontal layer heated from below, we can neglect the kinetic and potential energies, the energy of gravitation, and the dissipation comparing with the internal energy per unit volume U. We assume a Newtonian fluid and introduce the Boussinesq approximation. This means that all fluid properties, viz. the dynamic viscosity μ, the heat conductivity λ, and the density ρ are assumed to be constant, but only the temperature dependence of the density in the buoyancy term causing the thermal convection is taken into account. The linear thermal and caloric equations of state are assumed, where the pressure dependence is neglected. The equations are normalized by taking characteristic units: The height of the convection layer h_z, the thermal diffusion time h^2_z/κ, the temperature difference between the horizontal lower and upper boundaries T_1-T_2 and $(\rho\nu\kappa)/h^2_z$ for length, time, temperature and pressure, where κ the thermal diffusivity, ν the kinematic viscosity, and thus we obtain,

$$\nabla\cdot\mathbf{v}' = 0 \tag{4}$$

$$Pr^{-1}(\partial/\partial t' + v'\cdot\nabla)v' = -\nabla p' + \nabla^2 v' + RaT'e \tag{5}$$

$$(\partial/\partial t' + \mathbf{v}'\cdot\nabla)T' = \nabla^2 T' \tag{6}$$

Of course, the Prandtl number Pr, which is the ratio of momentum and heat transfer, and the Rayleigh number Ra, which is the ratio of potential and viscous energy, are the dimensionless parameters, defined as, respectively.

$$Pr = \nu/k, \text{ and } Ra = g\alpha h^3_z(T_1-T_2)/(\upsilon k) \tag{7}$$

It may be evident from (5) that for media with high Prandtl numbers Pr, the unsteady and non-linear terms play only a secondary role in comparison with the pressure, viscous, and buoyancy terms. With lower Prandtl numbers, however, these former terms play the important role.

For the practical application of the system of basic equations (4) – (6), it is critical to know in what range of parameters, the Boussinesq approximation is valid (Gray & Giorgini 1976). For the calculation of the onset of the steady cellular convection, we perform a perturbation analysis of the heat conduction condition. At the onset of convection, the velocities and temperature deviations are small, and thus the non-linear terms of the momentum and energy equation can be neglected. This assumption enables us to produce the steady, linear basic equations for the disturbance variables $\mathbf{v}^*$, T^*, and p^*:

$$\nabla\cdot v^* = 0 \tag{8}$$

$$0 = -\nabla p^* + \nabla^2 v^* + Ra\cdot T^*\cdot e \tag{9}$$

$$-w^* = \nabla^2 T^* \tag{10}$$

If we apply the curl twice to the momentum and energy equations, partial differential equations of the six order can be derived for the vertical fluctuation velocity w^* and the temperature deviation T^* using the continuity equation,

$$Ra\cdot \Delta_2 w^* = \nabla^6 w^* \tag{11}$$

$$Ra\cdot \Delta_2 T^* = \nabla^6 T^* \tag{12}$$

with

$\Delta_2 = \partial^2/\partial x^2 + \partial^2/\partial y^2$.

The relevant boundary conditions are:

$w^* = \partial^2 w^*/\partial z^2$ (free surface), $w^* = \partial w^*/\partial z$(rigid surface).

$T^*=0$(isothermal), $\partial T^*/\partial z=0$(adiabatic).

For the calculation of the onset of thermal cellular convection we follow Rayleigh (1916), and expand the solution of the partial differential equations (11) and (12) into a Fourier series, whose coefficients do not couple within the framework of linear stability theory. For infinite layers, the solution is separable, and the stability curve can be calculated analytically for free horizontal boundaries. However, in the case of rigid boundaries the eigenvalue equation must be solved numerically. Table 1 shows typical theoretical, numerical, and experimental results.

The parameters are the Rayleigh number Ra and the wave number $a=2\pi/L$. All solutions are unstable to small disturbances. The linear stability theory does not provide the critical values Rac, at which convection begins, but the additional consideration is required: For example, with increasing the Rayleigh number Ra, it reaches the minimum value of Rac=657, at ac=2.2, which determines the onset of thermal convection.

Linear stability theory, however, does not state how the solution evolves in the unstable area on the plane map, Ra vs. a. This is the area that the non-linear basic equations (4)-(6) may describe. As long as temperature dependence at free boundaries plays a part in an infinitely extended layer, there is ample possibility that hexagonal convection cells are formed, while in a cubic box with rigid four vertical and two horizontal boundaries longitudinal vortex rolls are generated . It is known that two-dimensional longitudinal convection rolls in parallel with shorter vertical boundaries are formed because of the lower friction (Zierep 1963, Masoud et al. 2018, Tighchi et al 2018). It may be, therefore, natural to conjecture that a unidirectional flow enhances to form the longitudinal convection rolls in the flow direction, but blocks to generate the transverse convection rolls with respect to the flow direction. This must be an intriguing interaction problem between the hexagonal convection rolls and the unidirectional shear flow.

The influence of shear flow on an extended Rayleigh-Bénard stability problem can be examined ideally in tilted convection boxes (Kirchartz 1980, Esfahani & Alinejad 2013a, b, Alinejad & Esfahani 2017): Speed of the basic flow can be easily varied by choice of the tilting angle of the box. At small tilting angles, the cellular hexagonal or pentagonal convection rolls begin to be transformed into longitudinal convection rolls in the primary direction of the basic flow. At increasing tilting angles, the speed of the basic flow becomes greater, so that its shear effect leads to a definite direction of convection rolls.

With increasing Rayleigh number Ra, the necessary heat transfer is unable to be achieved by two-dimensional convection rolls, so that the flow in the layer becomes three-dimensional. If the Rayleigh number Ra increases further, we reach the region of time-dependent oscillatory instabilities, and then turbulent cellular convection finally. By passing through these transitions, the amount of the heat transfer increases. As (5) infers, the transition to time-dependent instabilities takes place in a smaller Rayleigh number if the Prandtl number is small.

3.2. Experimental Method

The experiment is concerned with flow visualization with neutral buoyant particles, and measurements of flow velocity and heat transfer on thermal convection between two coaxial square containers, which are set horizontally and inclined by 45°, respectively.

Figure 7 shows a schematic diagram of the present horizontal experiment. The whole apparatus is placed in a constant-temperature chamber (2.20 m high, 3.45m wide, and 3.45m deep), in which the temperature can be controlled at any setting value in the range -30℃ ~ 80℃ ± 0.2℃. The dimension of the isothermal hot wall(inner heat transfer surface) is 100mm high, 100mm wide, and 50mm deep, while those of isothermal cold wall(outer heat transfer surface) are 110mm high, 110mm wide, and 50mm deep. The test section is a closed space between these two coaxial horizontal square containers so that the common gap is 5mm. Both of the containers are made of brass, having high thermal conductivity. The front and rear surfaces of the test section are made of transparent Plexiglas of 5mm thick.

In the present experiment, the test section is filled with distilled water, and the temperature at the inner surface is normally kept higher than that at the outer surface. The temperature at the outer surface is controlled by circulating the constant temperature water in the sinuous channel engraved in the wall of the outer cubic container, where the water temperature is precisely controlled at the setting value± 0.03℃. On the other hand, the temperature at the inner surface is maintained at the temperature of $25.0\pm\mathbf{0.05}$℃ by providing electric current in the heater covered with aluminum foil. The K-type thermocouples covered with silicon having the wire diameter of 0.1mm are used to monitor temperatures at the inner and outer surfaces, respectively. Each of the temperatures is an ensemble average of a total of 10 data recorded within one minute. A total of 30 thermocouples are used and are set along the inner and outer surfaces.

Figure 8 depicts a schematic diagram of the flow visualization. The flow in the test section is visualized using specially made tiny glass particles: In each the glass particle, there are air bubbles called “micro-balloons” in it so that the particle has a density of 1.01 g/cm^3. The mean diameter of the glass particle is of 50μm, and these particles are distributed homogeneously in the distilled water of the test section. The streak lines of the neutral buoyant particles within a Ne-He laser sheet have been photographed for a specified time duration. In the top-test section, there is a slit, so that the laser light can illuminate the particles within the sheet: this slit cuts vertically the plane symmetrical axis of the top-test section in parallel with the front face.

3.3. Experimental Results

Figure 9 draws the relations between the Nusselt number Nu and Rayleigh number Ra, where these numbers are defined:

$$Nu=Q_w\cdot d/\,(\Delta T\cdot A\cdot \lambda), \tag{13}$$

and,

$$Ra=g\cdot \beta\cdot \Delta T\cdot d^3/(\kappa\nu) \tag{14}$$

In Figure 9, another relation in the case of thermal convection between two infinitely large horizontal plates by Silveston (1958) is also shown for reference, in addition to the present horizontal and inclined by 45°cases. It is found that the critical Rayleigh number Ra for the onset of the thermal convection in the horizontal top-test section is equal to 1660 ± 97, where the result of uncertainty analysis in Section 4 is used to determine the value of 97. On one hand, in the inclined case by 45°, the critical Rayleigh number Ra_c in the top left-test section is smaller than 1300, though the relevant measurements Ra <1300 have not done. It may be worth noting that for the onset of the thermal convection between infinitely large two horizontal plates, the theoretical, critical Rayleigh number is 1708(Pellow & Southwell 1940), while the experimental critical Rayleigh number is 1700 ± 51(Silveston 1958). Figure 9 infers that the moving free boundary towards vertical direction at left and right sides, does not enhance the thermal convection in such a way that the heat transfer rate increases from the hot wall to the cold wall, but contributes to induce the longitudinal alternating vortices arranged in the top horizontal test section. On the one hand, by inclining the container by 45° with respect to horizontal, transfer rate of the heat is increased significantly, as shown in this figure, so that it is considered that the thermal convection in the top-left test section is enhanced.

Figure 10 illustrates streak lines and velocities at the left part in the top-test section within the slit, where the Rayleigh number Ra=1230, and $_0$the fluid volume flux between adjacent two streak lines q＝1.398mm^3/s. It may be evident that the velocity along the spiral curve of the vortex at the horizontal top test section is an order of 0.1 mm/s, while the velocity at the top of circulatory flow in the vertical left test-section is an order of 2 mm/s.

Figure 11 shows a flow visualization picture at the left-part in the top-section within the slit, where the Rayleigh number Ra=2120, and the camera shutter released time is of 60 seconds. In this figure, the thermal convection rolls arranged regularly may be discernible, though some are deformed by the mutual interaction among them.

Figure 12 shows flow visualization of the peak part of the upper-left test section of two coaxial square containers inclined 45° within the slit, where the Rayleigh number Ra=2260, and the shutter released time is of 60 seconds. It may be evident that there appear two paramount circulatory flows in the two coaxial square containers inclined by 45° with respect to the horizontal line. The left circulatory flow has the counter-clock-wise sense of rotation, while the right circulatory flow possesses the clock-wise-sense of rotation.

4. Uncertainty analysis

The total uncertainty in measured variables may be computed by the method of Kline & McClintock (1953). If F=F (v1, v2,…, vn) is the quantity to be measured, and δvi is the uncertainty in any specified variable vi. Then, the total uncertainty δF in the measurement is given by

$$\delta F = \left[\sum_{i=1}^{n} (\partial F/\partial v_i * \delta v_i)^2\right]^{1/2} \tag{13}$$

where each of the variable is assumed to be normally distributed: Each of the uncertainties should be quoted at the same odds. Eq. (13) gives the relation among the Nusselt number Nu and the measure variables, Q_w, d, ΔT, A, and λ. Then, assuming that each variable in (13) has an independent uncertainty, the total uncertainty of Nu is given by

$$\delta(Nu)/Nu= [(\delta Q_w/Q_w)^2+(\delta d/d)^2+(\delta\Delta T/\Delta T)^2+(\delta A/A)^2+(\delta\lambda/\lambda)^2]^{1/2} \tag{15}$$

In this relation, Q_w and λ are considered to be given, so that (15) reduces to

$$\delta(Nu)/Nu= [(\delta d/d)^2 +(\delta\Delta T/\Delta T)^2+(\delta A/A)^2]^{1/2} = [(\delta d/d)^2+(\delta\Delta T/\Delta T)^2+(\delta w/w)^2+(\delta h/h)^2]^{1/2} \tag{16}$$

where we use A=w·h.

When the variable uncertainties from Table 2 are substituted into (16), the uncertainty of Nusselt number is found to be

$$\delta(Nu)/Nu = [1\cdot 10^{-4}+25\cdot 10^{-4}+1\cdot 10^{-4}+1\cdot 10^{-4}]^{1/2}=\pm 5.29\ \%. \tag{17}$$

On the other hand, (14) gives the relation the Rayleigh number Ra and the variables, g, β, ΔT, d^3, κ , and ν . Then, again assuming that each variable in (14) has an independent uncertainty, the total uncertainty of Ra is given by

$$\delta(Ra)/Ra_{\max}=[(\delta\Delta T/\Delta T)^2+(3\delta d/d)^2]^{1/2} \tag{18}$$

When the uncertainties of the variables in Table 2 are substituted into (18), the uncertainty of Rayleigh number Ra is found to be

$$\delta(Ra)/Ra = [25\cdot 10^{-4}+9\cdot 10^{-4}]^{1/2}=\pm 5.83\ \% \tag{19}$$

Again the major contribution is from the temperature difference ΔT.

5. Discussion

In this section, the heat transfer rate, thermal conduction and convection in an inclined cubic box, where the lower wall is hotter than the upper wall, will be discussed with reference to Kirchartz's work in 1980.

It may be noteworthy that the flow sketch in Figure 13(a) clearly suggests that the colliding counter flow between the upwards and downwards two-dimensional Poiseuille flow satisfies the necessary conditions for the onset of Kelvin-Helmholtz instability along the dividing free streamline plane. In the interferometric picture, the white smeared portion in the central part may reflect the spiral rolling up of a protuberance on the plane surface of the discontinuity owing the instability (Fernando 1991).

Another interesting point in this picture may be the structure of longitudinal rolls in the inclined box, where the lower wall temperature is higher than the upper wall temperature. It may be evident that in the upwards two-dimensional Poiseuille flow, the temperature at the lower part is higher than that at the higher part in the flow, while in the downwards two-dimensional Poiseuille flow the temperature at the lower part is also higher than that at the higher part in the flow. In other words, the flow in the box is a circulatory flow consisting of two-layers; one is moving upwards, and the other is moving downwards, but the temperature in the flow decreases with the height from the lower hot wall to the upper cold wall.

Conclusion

In this section, the new knowledge and insights obtained through the present study are summarized:

1. The classical Rayleigh-Bénard problem of a horizontal fluid layer with different boundary conditions has been explored to acquire the basic knowledge on longitudinal vortex rolls in nature.

2. Conducted are two experiments on flow visualization with neutral buoyant particles, and measurements of flow velocity and heat transfer rate caused by the thermal convection between two coaxial square containers, which are set horizontal and inclined by 45°, respectively. It is found that the critical

Figure 1. Remarkable longitudinal parallel rows of white foams arranged in the direction of airflow over the sea surface. Photo was taken off Midway Island in Pacific Ocean on July 4, 1970.

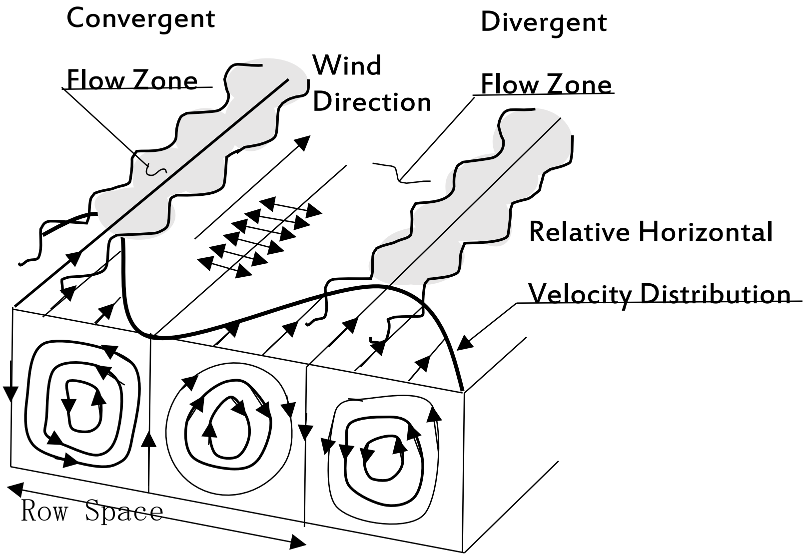

Figure 2. Schematic diagram for longitudinal Langmuir cells at the surface of the sea, visualized by the foams when the airflow over the surface exceeds to the critical velocity ca. 1m/s.

Figure 3. Longitudinal sand rolls on the surface of Libyan desert in Egypt.

This photo was taken by a satellite. Courtesy by NASA.

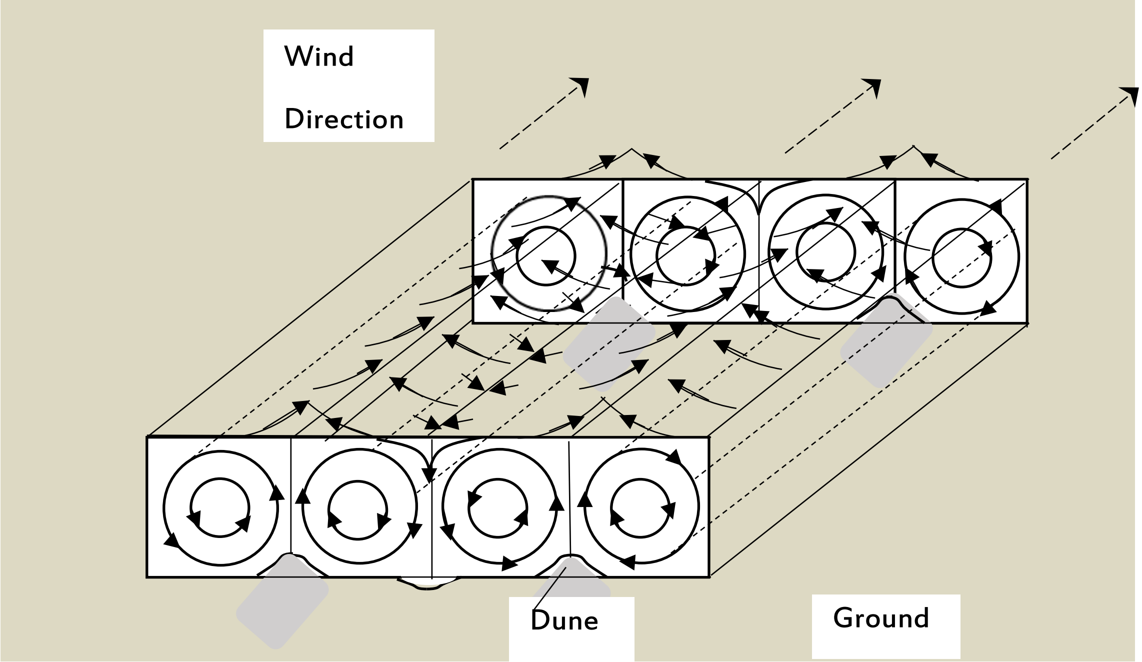

Figure 4. Hypothetical sketch of air circulation and longitudinal sand dunes over the desert.

Figure 5. Longitudinal vortex rolls delineated by white clouds in the atmosphere.
This photo was taken over Kyrgyzstan through the window of airplane on the way to Istanbul on May 25, 2012.

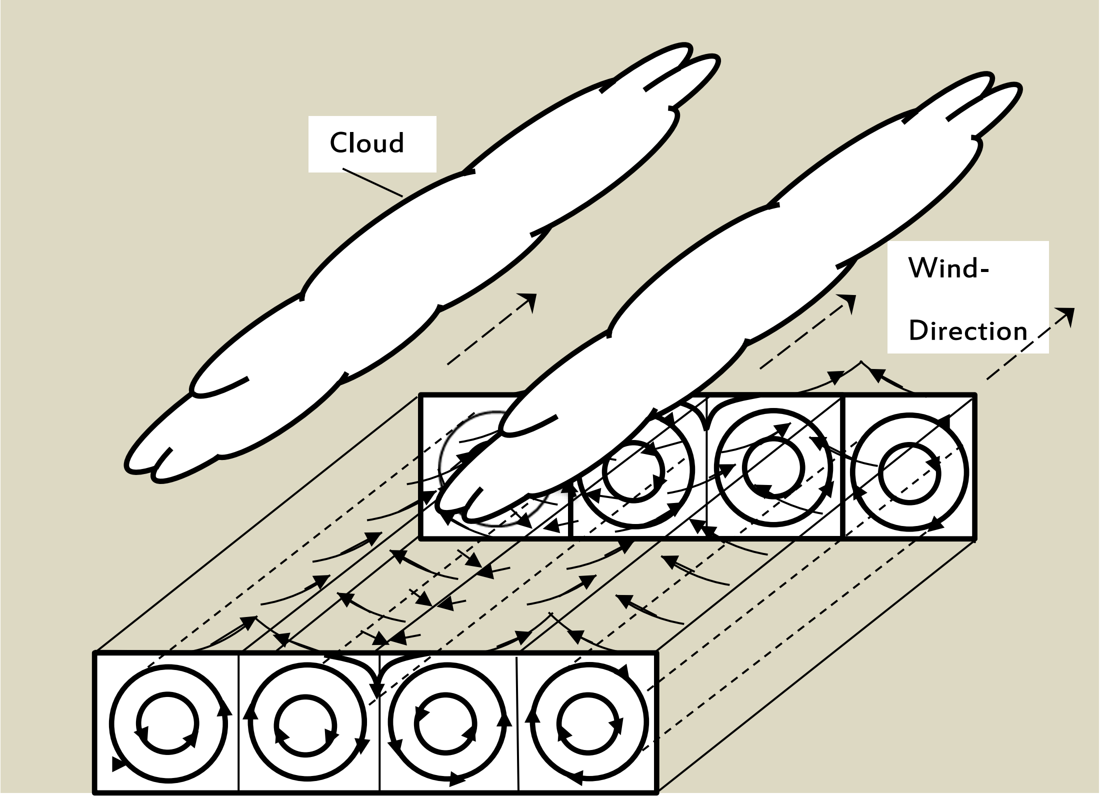

Figure 6. Hypothetical sketch of cloud streets and longitudinal air circulation.

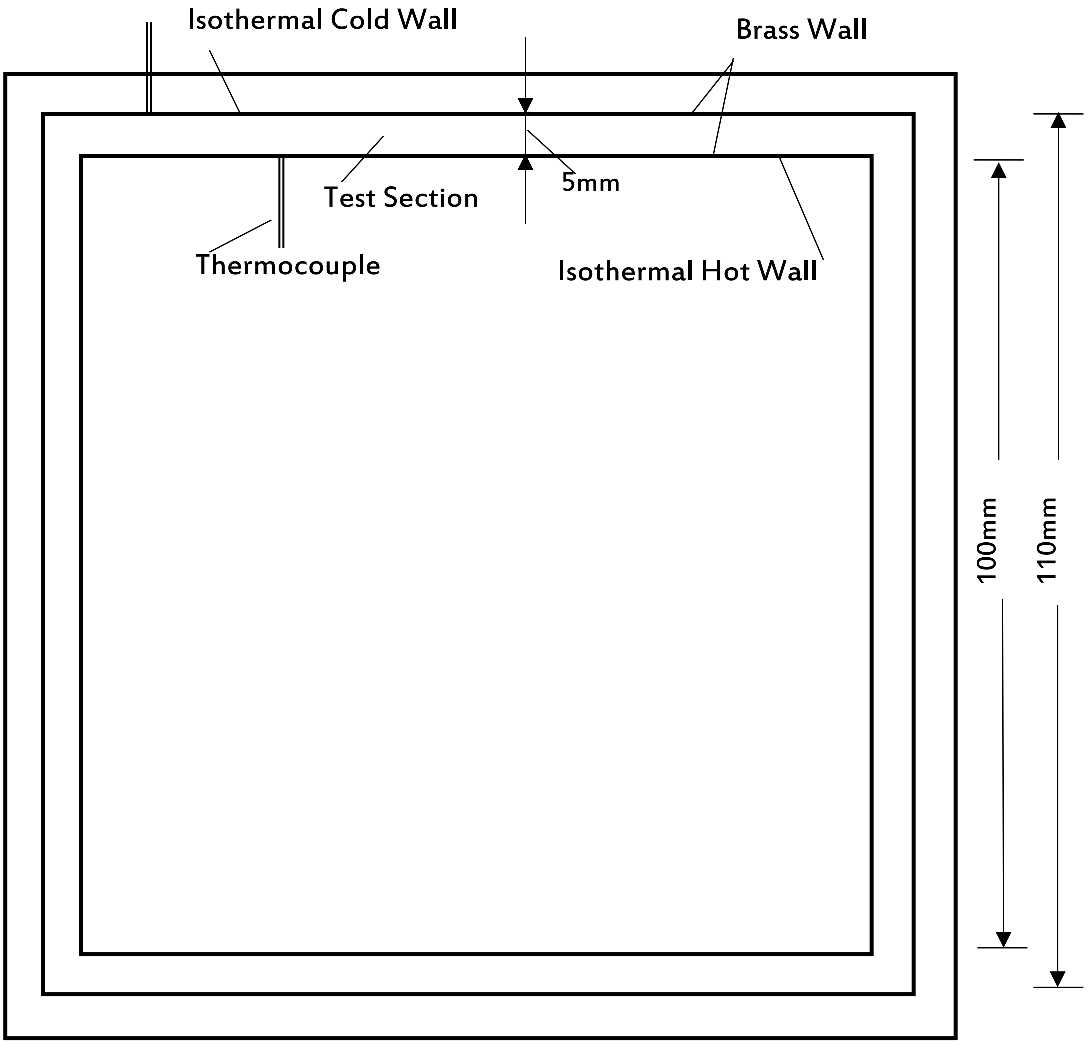

Figure 7. Schematic diagram of the present horizontal experiment. Cross sectional view of the test section.

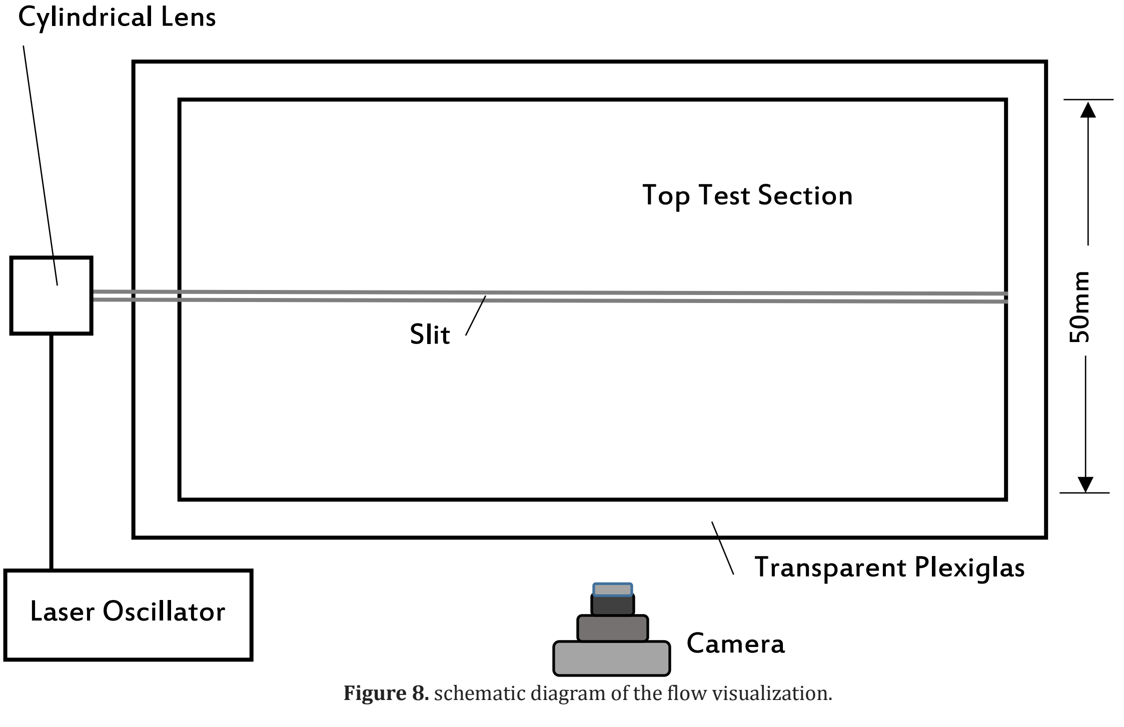

Figure 8. schematic diagram of the flow visualization.

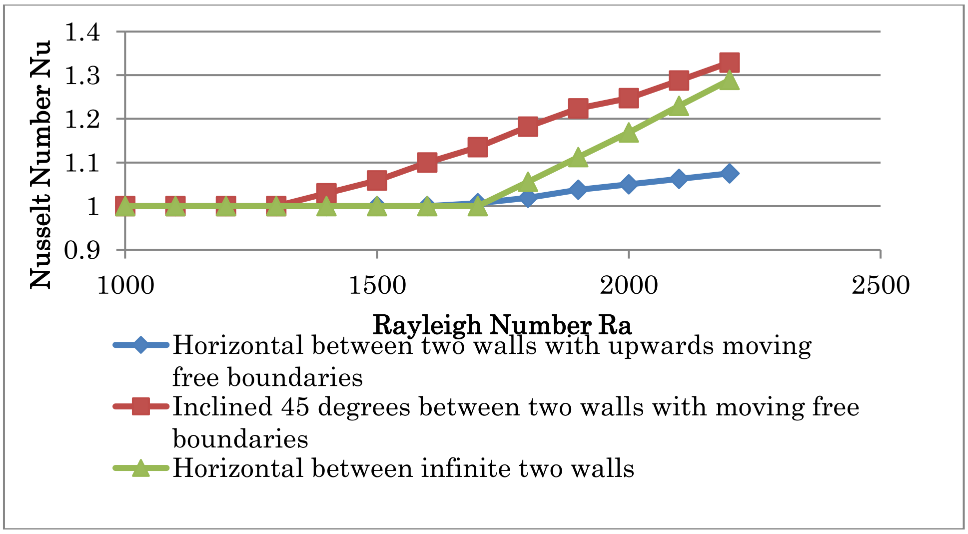

Figure 9. Nusselt number Nu against Rayleigh number Ra.

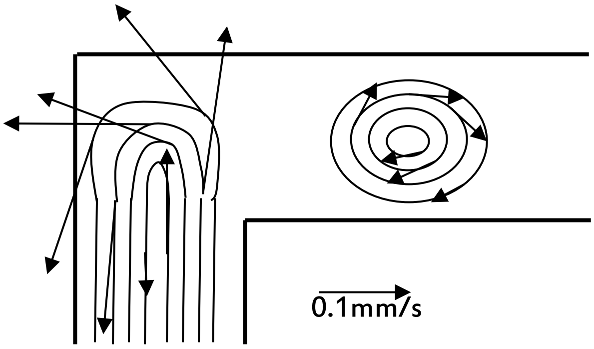

Figure 10. Streak lines and velocities at the left part in the top-test section within the slit.

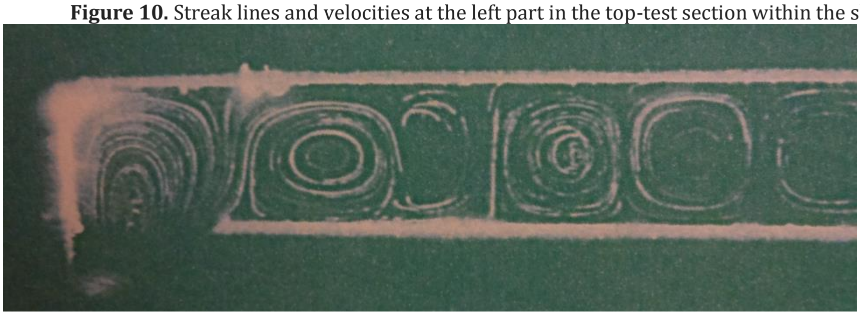

Figure 11. Flow visualization picture at the left-part in the top-section within the slit.
Rayleigh number Ra=2120, and camera shutter released time= 60 seconds.

Figure 12. Flow visualization of the peak part of the upper-left test section of two coaxial square containers inclined 45° within the slit.
Rayleigh number Ra=2260, and shutter released time= 60 seconds.

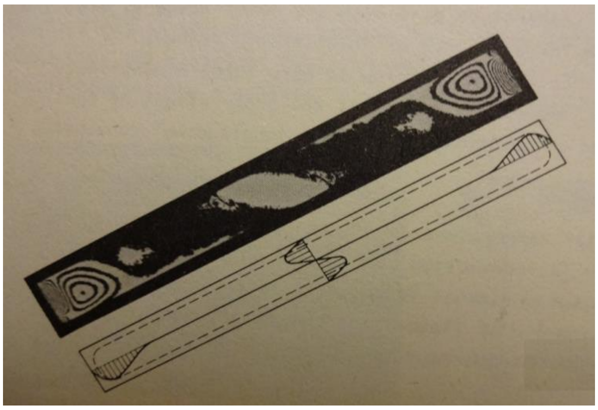

(a) Interferometric picture within vertical cross-section of an inclined box, together with the flow sketch.

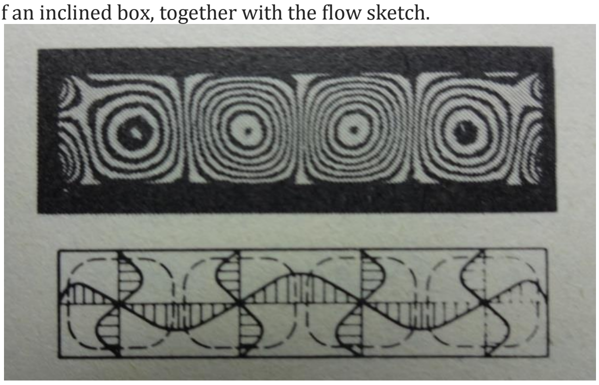

(b) Interferometric picture within transverse cross section of the inclined box, together with the flow sketch.

Figure 13. Interferometric pictures of longitudinal convection rolls in an inclined box. Fluid: silicone oil, Prandtl number=1780. After Kirchartz(1980).

Table 1. List of critical Rayleigh and wave numbers for instability of infinite horizontal fluid layer between upper and lower boundaries.

Lower boundary	Upper boundary	Critical Rayleigh number	Critical wavenumber
free	free	657	2.2
rigid	free	1101	2.7
rigid	rigid	1707.8	3.1
Pellow & Southwell 1940(theory)			
rigid	rigid	1700±51	
Silveston 1958(experiment)			
rigid	rigid	1660±97	
With free upwards moving boundary at each of sides.		Nakagawa et al. 1998(experiment)	

Table 2. Mean value and uncertainty interval of variable.

Variable	Mean	Uncertainty interval
d	5(mm)	±0.01
ΔT	25(℃)	±0.05
w	100(mm)	±0.01
h	50(mm)	±0.01

Rayleigh number Rac for the onset of the thermal convection in the horizontal top-section is equal to 1660±97, whereas in the inclined by 45° top left test-section, it is smaller than 1300, though the relevant measurements Ra <1300 have not done.

3. The moving free boundaries towards upwards direction at the left and right side, respectively, don't enhance the thermal convection in such a way that the heat transfer rate in the vertical direction increases from the hot wall to the cold wall, but contributes to induce the longitudinal alternating vortices arranged in the horizontal top test-section. On the one hand, by inclining the coaxial square containers by 45° with respect to horizontal line, the heat transfer rate or Nusselt number Nu is significantly increased so that the thermal convection in the top left-section is enhanced.

4. It is found by the flow visualization with neutral buoyant particles in fluids that the flow velocity in the vertical left test-section is in order of 2 mm/s, while the velocity along the spiral curve of the vortex at the left end of the horizontal top test-section is in order of 1 mm/s.

5. It is realized that the thermal convection rolls arranged regularly in the horizontal top test-section are interacting with adjacent rolls, so that the arrangement is unsteady.

6. It has been confirmed by the present flow visualization that there appear two paramount circulatory flows in the coaxial square containers inclined by 45° with respect to horizontal line: One is in the top left-section, having the counter-clock-wise sense of rotation, while the other is in the top right test-section, having the clock-wise sense of rotation. This must be the primary reason why transfer rate of the heat is significantly increased comparing with that of the horizontal case.

7. It is suggested that longitudinal rolls in nature, viz. Sea, desert, and atmosphere are generated by the essentially same mechanism as those in the laboratory, though the former boundary conditions are often difficult to specify exactly.

Nomenclature

$a=2\pi/L$	wave number
$A=w.h$	total heat transfer area of the hot wall
d	gap between hot and cold walls
$e=(0, 0, 1)$	unit vector
g	gravitational acceleration
h	depth of the hot wall
h_z	height of the convection layer
h^2_z/κ	thermal diffusion time
L	wavelength
Nu	Nusselt number
p	pressure
Pr	Prandtl number
q	heat flux
^{0}q	fluid volume flux between adjacent two streak lines
Q_w	heat flux through the working fluid in the test section
Ra	Rayleigh number
t	time
$\Delta T = T_1 - T_2$	temperature difference between hot and c walls
T^*	temperature deviation
U	internal energy per unit mass
v (u, v, w)	velocity vector in the left hand coordinate system
w	width of the hot wall
w^*	vertical fluctuation velocity
Greek symbol	
ρ	density of fluid
τ	shear stress tensor
μ	dynamic viscosity of the fluid
ν	kinematic viscosity of the fluid
κ	thermal diffusivity
λ	coefficient of thermal conductivity
β	coefficient of volume expansion
∇p	pressure gradient
$\nabla \cdot q$	divergence of the heat flux vector
[ ]	tensor products

References

[1] Akiyama, M., Hwang, G.L., Chang, K.C. (1971) Experiments on the onset of longitudinal vortices in laminar forced convection between horizontal planes. J. Heat Transfer 93, 335-341.

[2] Alinejad, J., Esfahani, J.A. (2017) Taguchi design of three dimensional simulations for optimization of turbulent mixed convection in a cavity, Meccanica , 52 , 925-938

[3] Bird, R.B., Stewart, W.E., Lightfoot, E.N. (1960) Transport Phenomena. Wiley & Sons, New York.

[4] Chang, M.Y., Yu, C.H., Lin, T.F.(1997) Changes of longitudinal vortex roll structure in a mixed convective air flow through a horizontal plane channel; an experimental study. Int. J. Heat and Mass Transfer 40, 347-363.

[5] Chiu, K.C., Rosenberger, F. (1987) Mixed convection between horizontal plates-Entrance affects. Int. J. Heat Mass Transfer 30, 1645-1654.

[6] Esfahani, J.A., Alinejad, J. (2013a) Entropy generation due to conjugate convection in an enclosure using the lattice Boltzmann method, Journal of Thermophysics and Heat Transfer , 27, 498-505

[7] Esfahani, J.A., Alinejad, J. (2013b) Lattice Boltzmann simulation of turbulent natural convection: enclosure heated from below. Journal of Thermophysics and Heat Transfer, 31, 910-919

[8] Fernando, H.J.S. (1991) Turbulent mixing in stratified fluids. Annual Review of Fluid Mechanics 23, 455-493.

[9] Gray, D.D., Giorgini, A. (1976) The validity of the Boussinesq approximation. Int. J. Heat Mass Transfer, 19, 545-551.

[10] Helga, B. (2008) The Great Sand Sea in Egypt: Formation, dynamics and Environmental Change: A sediment Analytical approach. Elsevier, Amsterdam, 1-3.

[11] Kirchartz, K.R. (1980) Zeitabhängige Zellularkonvektion in horizontalen und geneigten Behältern. Ph.D thesis, Universität Karlsruhe.

[12] Kline, S.J., McClintack, F.A. (1953) The description of uncertainties in single sample experiments. Mechanical Engineering, 3.

[13] Komatani, Y., Ostrach, S. (1976) Effect of thermal instability on thermally developed laminar channel flow. J. Heat Transfer 98, 62-66.

[14] Komatani, Y., Ostrach, S., Miao, H. (1979) Convection heat transfer augmentation in thermal entrance regions by means of thermal instability. J. Heat Transfer 101, 222-226.

[15] Laein, R.P., Rashidi, S., Estani, J.A.(2016) Experimental investigation of nano-fluid free convection over the vertical and horizontal flat plates with uniform heat flux by PIV , Advanced Powder Technology, 27 , 312-322

[16] Lee, F.S., Hwang, G.J. (1991) Transient analysis on the onset of thermal instability in thermal entrance region of a horizontal parallel plate channel. J. Heat Transfer 113, 363-370.

[17] Masoud, S., Tighchi, S., Ahmadi, H., Abolfazi, E.J.(2018) Taguchi optimization of combined radiation/natural convection of participating medium in a cavity with a horizontal fin using LBM , Physica A: Statistical Mechanics and its Applications. 509, 1062-1079

[18] Nakagawa, T.R.M., Higashi, K., Funawatashi, Y., Suzuki, T. (1998) Thermal convection between coaxial horizontal square containers. Acta Mechanica, 128, 183-199.

[19] Nakagawa, T. R., Suzuki, T. (2001) On thermal convection between two coaxial square containers inclined by 45°. Int. J. Heat and Mass Transfer 37, 1-4.

[20] Oertel, H. Jr. (1982) Thermal instabilities. In: Convective Transport and Instability Phenomena, G. Braun, Karlsruhe, 3-24.

[21] Ostrach, S., Komatani, Y. (1975) Heat transfer augmentation in laminar fully developed channel flow by means of heating from below. J. Heat Transfer 97, 220-225.

[22] Pellow, A., Southwell, R.V. (1940) On maintained convective motion in a fluid heated from below. Proc. R. Soc. London, A176, 312-343.

[23] Quazzani, M.T., Caltagirone, J. P., Meyer, G., Mojtabi, A.(1989) Numérique et experimental de la convection mixte entre deux plans horizontaux a temperatures differents. Int. J. Heat Mass Transfer 32, 261-269.

[24] Quazzani, M.T., Platten, J.K., Mojtabi, A. (1990) Etude experimental de la convection mixte entre deux plans horizontaux a temperatures differents-Ⅱ. Int. J. Heat Mass Transfer 33, 1417-1427.

[25] Rayleigh, Lord (1916) On convection currents in a horizontal layer of fluid, when the higher temperature is on the underside. J. Science, 32, 529.

[26] Silveston, P.L. (1958) Wärmedurchgang in waagerechten Flüssigkeitsschichten. Teil 1. Forsch. Ing. Wes. 24, 29-32, 59-69.

[27] Tighchi, H.A.,Sohani, M., Esfahani, J.A.(2018) Effect of volumetric radiation on natural convection in a cavity with a horizontal fin using lattice Boltzmann method , European Physical Journal Plus , 33 , 2018-3.

[28] Zirep, J. (1963) Zur Theorie der Zellularkonvektion: Zellularkonvektions-strömungen in Gefäβen endlicher horizontaler Ausdehnung. Beitr. Phys. Atmos. 36, 70-76.